ONLINE FIRST June 25, 2026

Computer Assisted Methods in Engineering and Science
***, https://doi.org/10.24423/cames.2026.1847

Predicting Velocity and Pressure Distributions in Cyclone Systems: A Novel Combined CFD-ANN Approach

Ahmad Indra Siswantara[1)], Illa Rizianiza[1),2)*], Ridho Irwansyah[1)], Sulaksana Permana[3)], Fadil Naufal Wahas[1)], Adi Syuriadi[1),4)], M. Hilman Gumelar Syafei[1),5)]

[1)] *Mechanical Engineering, Faculty of Engineering, Universitas Indonesia, Depok, West Java, Indonesia*
[2)] *Mechanical Engineering, Faculty of Engineering and Industrial Technology, Institut Teknologi Kalimantan, Balikpapan, Kalimantan Timur, Indonesia*
[3)] *Mechanical Engineering, Faculty of Industrial Technology, Universitas Gunadarma, Depok, West Java, Indonesia*
[4)] *Mechanical Engineering, Politeknik Negeri Jakarta, Depok, West Java, Indonesia*
[5)] *Mechanical Engineering, Faculty of Engineering, Universitas Negeri Semarang, Semarang, Jawa Tengah, Indonesia*

[*] *Corresponding Author: illa.rizianiza@ui.ac.id*

This study uses computational fluid dynamics (CFD) with the k-ε turbulence model and an artificial neural network (ANN) to analyze cyclone flow. The results show that the pressure drop rises from 0.90 kPa to 6.54 kPa for inlet velocities of 7 m/s to 20 m/s. The ANN predicts the pressure drop with a 4.3 % error. The CFD-ANN approach improves insight into cyclone design.

Keywords: artificial neural network, cyclone, computational fluid dynamics, pressure drop, prediction.

1. Introduction

Cyclone separators are critical unit operations in process industries for gas–solid separation, offering high collection efficiency ($>98\,\%$ for particles larger than $5\,\mu$m) [1], robustness [2], and low maintenance [3]. Their performance is governed by the three-dimensional distributions of velocity and static pressure, which dictate particle trajectories, vortex stability, and flow phenomena such as vortex core precession [4].

Recent advancements in cyclone separator research have increasingly relied on high-fidelity CFD to resolve the strongly swirling and anisotropic turbulent structures governing cyclone performance. Soliman *et al.* [5] demonstrated that streamlined inlet and outlet ports can substantially reshape the velocity field and reduce energy losses, underscoring the sensitivity of cyclone hydrodynamics to geometric refinements. Complementary large-eddy simulation (LES) investigations by Brar and Rahmani [6] further revealed the strong influence of operating temperature on vortex instability and the precessing vortex core, indicating that thermally driven variations can fundamentally alter the pressure and velocity distributions within the cyclone. In parallel, Wasilewski *et al.* [7] showed that modifications to the central-rod geometry significantly affect separation efficiency and pressure drop, emphasizing the nonlinear interplay between geometric parameters and turbulent flow development. Additionally, Parvaz *et al.* [8] reported that changes in gas exhaust geometry markedly influence internal flow patterns, erosion behavior, and overall cyclone performance, further illustrating how geometric perturbations propagate through the velocity and pressure fields. Despite its accuracy, CFD remains computationally expensive and impractical for rapid design or real-time prediction. These limitations motivate the development of hybrid CFD-ML (machine learning (ML)) approaches capable of retaining physical fidelity while reducing computational burden, a direction in which the present study advances the state of the art.

To mitigate these limitations, data-driven surrogate models and hybrid CFD-ML approaches have gained traction. ANNs capture nonlinear relationships and enable fast prediction once trained [9]. In cyclone applications, hybrid models have successfully predicted scalar performance indicators, such as pressure drop [10], cut-off diameter [11], collection efficiency under varying operating conditions [12], and optimal geometric parameters [11]. However, these studies remain restricted to global or integrated quantities and do not reconstruct the complete multicomponent velocity U_x, U_y, U_z and pressure fields across the entire domain. Physics-informed neural networks (PINNs) incorporate physical constraints but remain limited for representing highly anisotropic cyclone flows [13], yet their application to highly anisotropic cyclone flows with strong vortex breakdown and secondary circulations remains limited and computationally distinct from those of pure data-driven surrogates.

This study introduces a novel ANN-based surrogate model that predicts the full three-dimensional velocity and static pressure fields in a cyclone separator with a helical inlet, trained exclusively on high-fidelity CFD datasets. Unlike previous hybrid approaches, the proposed model delivers spatially resolved, multicomponent flow-field reconstruction with mesh-independent performance. A systematic investigation evaluates data sampling strategies, training dataset size, mesh-resolution effects, and extrapolation limits beyond the training enve-

lope. This represents a purely data-driven ANN surrogate for full-field prediction in cyclone systems, achieving millisecond-scale prediction time with CFD-level accuracy. The developed framework offers a computationally efficient tool for rapid design iteration, sensitivity analysis, and deeper insight into complex gas–solid flow structures in industrial cyclones.

2. Methods

2.1. CFD simulation

CFD simulation of the cyclone was conducted under steady-state, isothermal, and turbulent conditions, using the k-ε turbulence model. The steady-state assumption implies that flow properties: velocity, pressure, and temperature do not change over time. Although cyclone flows can exhibit unsteady and swirling characteristics, steady-state simulations were chosen primarily to capture the average flow patterns and pressure distribution efficiently while maintaining computational feasibility. Transient simulations, although more physically accurate, require significantly higher computational resources and may provide limited additional insight for engineering design purposes, where time-averaged flow characteristics are the main concern [14]. Steady-state CFD simulations have been successfully applied in cyclone studies; for instance, Meza *et al.* [15] demonstrated that steady-state modeling can reliably predict mean flow patterns and pressure drop in cyclone separators.

The flow within the cyclone is turbulent, and the k-ε turbulence model is widely used to simulate this behavior due to its robustness, computational efficiency, and reasonable accuracy in predicting mean flow quantities such as pressure drop and separation efficiency. The standard k-ε model solves transport equations for turbulent kinetic energy and its dissipation rate, effectively capturing mean flow properties under turbulent conditions. More advanced models, such as Reynolds stress models (RSM) or LES, can capture anisotropic or transient turbulence with higher accuracy but require substantially greater computational effort and longer simulation times [16]. Steady-state simulations with the k-ε model are common in cyclone studies focused on design and performance optimization and have shown good agreement with experimental data for pressure drop and velocity distributions in such systems. This modeling approach balances computational efficiency and reliability for industrial cyclone design applications. The objectives of this study are to assess the influence of inlet velocity on pressure drop and to generate training data for a CFD-ANN surrogate model. For this purpose, the k-ε model provides a practical balance between accuracy and computational efficiency. Previous studies have shown that, for particle-laden cyclone flows, the k-ε model can reliably predict global flow behavior and pressure-drop trends, although it may underestimate local anisotropy

or secondary flows [17]. The CFD results were validated against experimental measurements. This validation confirmed that the selected model provides predictions with a reasonable error margin, making it suitable for engineering applications and ANN training. To systematically investigate the effect of varying inlet velocity, four simulation schemes were defined, as shown in Table 1. This approach allows a detailed analysis of the pressure and velocity distributions within the cyclone and the connected helical pipe while maintaining computational efficiency.

Table 1. Simulation schemes with varying inlet velocities.

Scheme	Inlet 1 velocity [m/s]	Inlet 2 velocity [m/s]
1	7	1
2	10	1
3	13	1
4	20	1

2.2. Boundary conditions

The following boundary conditions are given:

- Inlet 1 (exhaust gas from the internal combustion engine (ICE)): exhaust gas enters through Inlet 1 at velocities of (7, 10, 13, and 20) m/s. This gas carries particles that require separation.
- Inlet 2 (pyrolysis gas from reactor): Inlet 2 is utilized for the introduction of pyrolysis gas generated by the pyrolysis reactor, which is maintained at a constant velocity of 1 m/s.
- Outlet 1 (cyclone gas): the cleaned gas that has been separated from the particles exits through Outlet 1, which also serves as the exit point for the gas leaving the cyclone.
- Outlet 2 (cyclone particles): particles separated from the gas are collected and discharged through Outlet 2. This outlet is typically located at the bottom of the cyclone to leverage gravitational forces in the removal of the particles.
- Wall 1 (outer wall of the cyclone): this wall, which forms the outer boundary of the cyclone, serves to contain the pressure of the gas and particles within the apparatus.
- Wall 2 (inner wall): the inner wall at the top of the cyclone functions to regulate the gas flow and assist in the separation process.

2.3. Mesh independency study

A structured hexahedral mesh was used (Fig. 1). Hexahedral structured grids have demonstrated advantages in numerous studies. However, the creation of

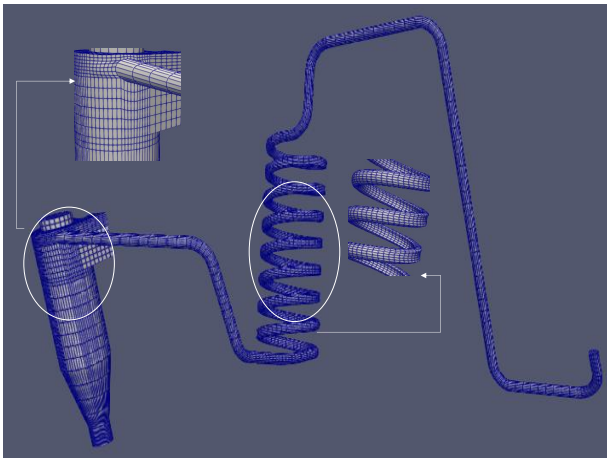

FIG. 1. Hexahedral mesh with a zoomed-in view of the cyclone and helical regions.

these grids requires a manual process that consumes significant time and effort [18]. Using hexahedral meshing in CFD simulations offers several advantages over other types of meshes, such as tetrahedral or polyhedral meshes. First, hexahedral meshes often provide more accurate results due to their regular shape, which allows for better definition of flow gradients. Additionally, hexahedral elements tend to offer higher numerical stability, reducing numerical oscillations and improving solution convergence, especially in complex problems [19]. Computational efficiency is also a key advantage, as hexahedral meshes typically require fewer elements to achieve a certain level of accuracy, thus reducing computation time. While generating hexahedral meshes can be more challenging for complex geometries, techniques such as domain decomposition can make this process more efficient for specific problems. Furthermore, hexahedral meshes can yield smoother and more representative solutions of the physical phenomena being analyzed, with fewer voids that can enhance flow analysis and pressure distribution. Lastly, applying boundary conditions is often easier with hexahedral meshes due to the more structured nature of the elements, allowing for better control over flow and environmental conditions. Therefore, hexahedral meshing is often considered a superior choice when accuracy and efficiency are prioritized in CFD simulations.

Figure 2 shows the relationship between cell number and pressure drop. Increasing the number of cells from 98 322 to 270 579 significantly increases the predicted pressure drop, while beyond 270 579 cells, variations become marginal, with values rising slightly from 1.76 kPa to 1.90 kPa at 339 487 cells, indicating convergence. Therefore, a mesh of approximately 270 000 cells was selected, as further refinement does not significantly improve accuracy but increases computational cost.

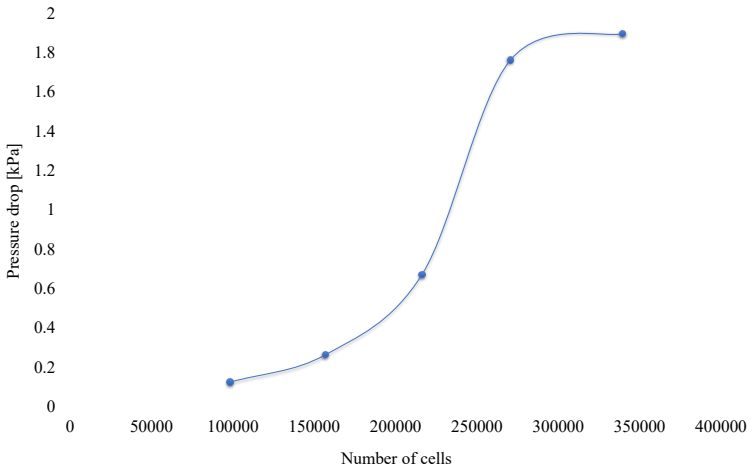

Fig. 2. Pressure drop versus cell count for the mesh independence test.

2.4. ANN model

ANNs have received increasing attention for their ability to capture nonlinear flow–property relationships and reproduce CFD outputs at a fraction of the computational cost [20]. Their use as surrogate models has been demonstrated across various CFD applications, including hydrodynamics, multiphase flows, and external aerodynamics. For instance, Dhakane *et al.* [21] employed a deep neural network (DNN) to predict hydrodynamic parameters in bubble-column simulations using inlet velocity and spatial coordinates as inputs, achieving $R^2 > 0.97$. Kaak *et al.* [22] applied a CFD-ANN strategy to optimize plunger-valve performance, while Diop *et al.* [23] utilized a 21-layer ANN with 512 neurons per layer to reconstruct wake dynamics behind a high-rise building using probe-based velocity inputs. Tian *et al.* [24] further demonstrated the predictive capability of nested DNNs for wind pressure coefficients, obtaining correlation coefficients above 0.996. Despite these developments, ANN-based surrogate modeling for complex cyclone–helix geometries remains limited, particularly for reconstructing multicomponent velocity and static pressure fields. Motivated by this gap, the present study develops a hybrid CFD-ANN surrogate trained directly on high-fidelity CFD results to predict U_x, U_y, U_z, and p at arbitrary spatial coordinates within the cyclone domain (Fig. 3).

In this work, the ANN model takes as inputs the three inlet velocity components $U_{x,\mathrm{in}}$, $U_{y,\mathrm{in}}$, $U_{z,\mathrm{in}}$ and the spatial coordinates x, y, z. The network outputs are the corresponding local velocity components U_x, U_y, U_z and static pressure p. From the four CFD schemes, approximately 127 000 data points were exported; these were randomly downsampled to ∼30 000 points to reduce computational load while maintaining spatial representativeness (Fig. 4).

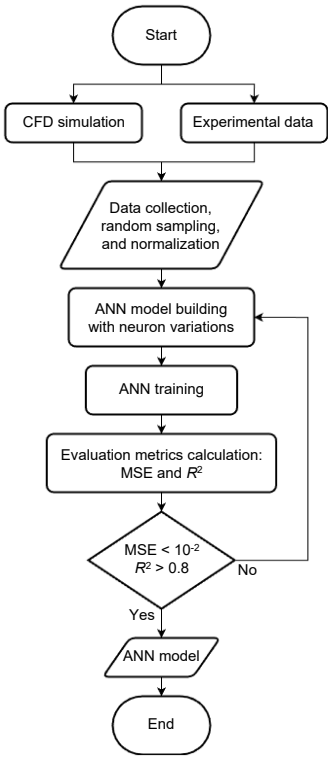

FIG. 3. Workflow of the CFD-ANN methodology.

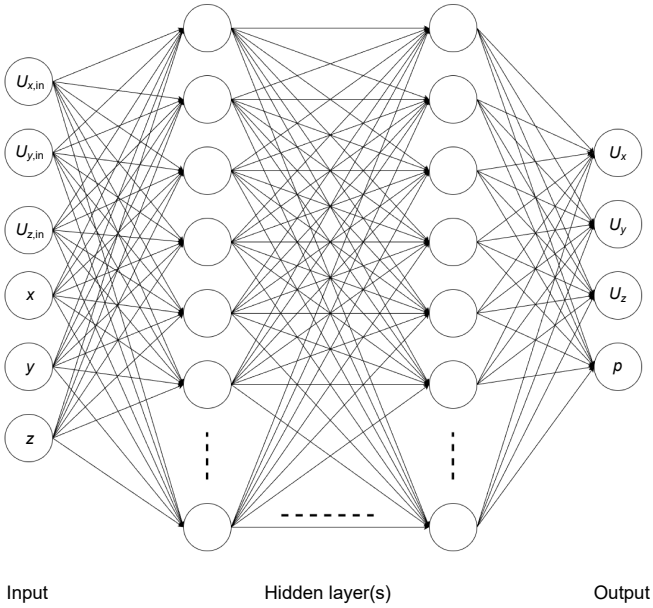

FIG. 4. ANN architecture used for flow prediction.

Dataset preprocessing. Prior to training, the dataset underwent several preprocessing steps:

(i) screening for missing entries, numerical spikes, or mesh-interpolation artifacts–no data were removed since all CFD fields were converged and physically consistent;

(ii) shuffling to eliminate ordering bias;

(iii) Min–Max normalization of all inputs and outputs to the [0, 1] range to mitigate activation saturation and stabilize gradient descent;

(iv) an 80 %–10 %–10 % split into training, validation, and testing datasets.

Network architecture and hyperparameter tuning. The ANN uses a fully connected feed-forward architecture with three hidden layers containing 128, 64, and 64 neurons, respectively. These layer sizes were determined through empirical hyperparameter tuning using grid search and validation performance to balance predictive accuracy and computational efficiency. Rectified linear unit (ReLU) activation functions were employed in hidden layers, while the output layer used linear activation for continuous outputs. The network was trained using the Adam optimizer [25, 26] with a learning rate of 1×10^{-3} and a batch size of 256. These hyperparameters were chosen based on iterative experimentation: smaller learning rates caused slower convergence, larger learning rates destabilized training, and batch sizes smaller than 128 led to noisy gradient updates. The model was trained for 500 epochs, with early stopping (patience = 20 epochs) used to avoid overfitting. L2-regularization ($\lambda = 10^{-4}$) further improved generalization.

Computational environment and reproducibility. All ANN modeling was implemented in Python using TensorFlow 2.20 and executed on an Intel®Core™ i9-12900H (14-core, 20-thread) processor. The library versions, hardware, and multithreading configuration are reported to ensure full reproducibility.

Model evaluation. Performance was assessed using mean squared error (MSE) and the coefficient of determination R^2, as defined in Eqs. (1) and (2), to quantify both absolute prediction error and overall goodness-of-fit. Cross-validation was performed by rotating the training, validation, and test sets to confirm model robustness against dataset variations:

$$\mathrm{MSE} = \frac{1}{n}\sum_{i=1}^{n}\left(y_{\mathrm{actual},i} - y_{\mathrm{predicted},i}\right)^2, \tag{1}$$

$$R^2 = 1 - \frac{\sum_{i=1}^{n}\left(y_{\mathrm{actual},i} - y_{\mathrm{predicted},i}\right)^2}{\sum_{i=1}^{n}\left(y_{\mathrm{actual},i} - \overline{y}_{\mathrm{actual}}\right)^2}. \tag{2}$$

3. Results and discussion

3.1. Simulation

The static pressure distribution along the helical pipe, as shown in Fig. 5 and quantified in Table 2, demonstrates that curvature-induced secondary flows and wall shear are the primary contributors to total pressure loss. In case 1, the inlet velocity at inlet 1 is 7 m/s, resulting in a total pressure drop of 0.902 kPa (≈9.02 mbar). The pressure declines sharply along the first helical turn, reflecting the development of Dean vortices and enhanced wall friction. Case 2, with a higher inlet velocity of 10 m/s, produces a ΔP of 1.762 kPa (≈ 17.62 mbar), showing more pronounced secondary flows and stronger turbulence dissipation. Case 3, at 13 m/s, exhibits a pressure drop of 2.888 kPa (≈28.88 mbar), while case 4, with the highest inlet velocity of 20 m/s, generates the largest loss, $\Delta P \approx$ 6.540 kPa (≈65.40 mbar). These results indicate that the helical pipe accounts for the majority of system losses, and the pressure drop increases nonlinearly with inlet velocity due to enhanced Dean vortex activity, curvature effects, and turbulence amplification.

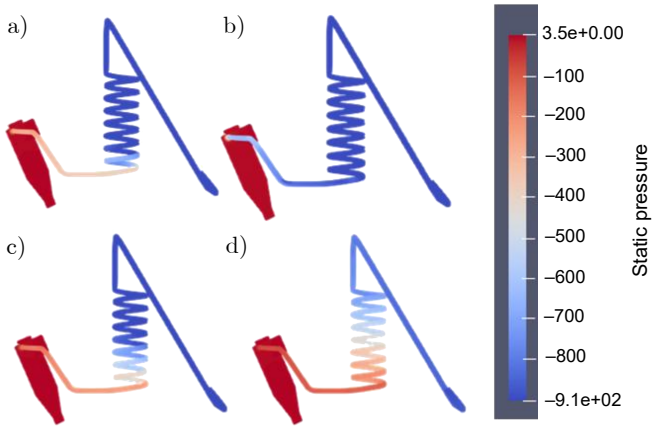

Fig. 5. Contours of static pressure [kPa] obtained from CFD simulations for four different inlet velocity schemes: a) scheme 1, b) scheme 2, c) scheme 3, and d) scheme 4.

Table 2. Boundary condition.

Scheme	Boundary condition						Pressure drop [kPa]
	Inlet 1 [m/s]	Inlet 2 [m/s]	Outlet 1 [m/s]	Outlet 2 [m/s]	Wall 1 [m/s]	Wall 2 [m/s]	
1	7	1	0	0	0	0	0.90245
2	10	1	0	0	0	0	1.76213
3	13	1	0	0	0	0	2.88804
4	20	1	0	0	0	0	6.53999

Velocity contours within the cyclone, presented in Fig. 6, further reveal the influence of inlet momentum on vortex formation. In case 1, the flow exhibits peak velocities of 8–10 m/s near the inlet, decaying to 1–2 m/s at the vortex core, indicative of incomplete swirl establishment. Case 2 demonstrates stronger rotation, with high-velocity zones (≈10–12 m/s) near the cyclone walls and a stabilized core (1–3 m/s). In case 3, increased turbulence and wall friction reduce the overall velocity to 2–5 m/s, and in case 4, despite the highest inlet momentum, large regions of the cyclone experience velocities below 2 m/s. This demonstrates that turbulent dissipation dominates over convective transport at high inlet velocities, leading to a counterintuitive reduction of effective swirl velocity within the cyclone core.

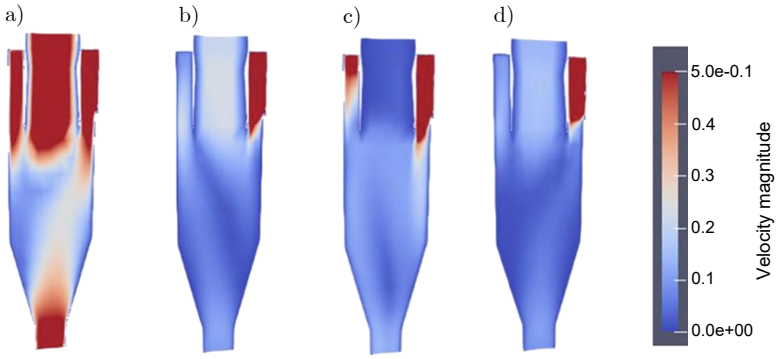

Fig. 6. Contours of velocity magnitude [m/s] inside the cyclone obtained from CFD simulations for four different inlet velocity schemes: a) scheme 1, b) scheme 2, c) scheme 3, and d) scheme 4.

The static pressure field inside the cyclone, illustrated in Fig. 7, aligns with the velocity trends. Case 1 exhibits a negative-pressure core (≈ −0.8 to −1.0 mbar) with mildly positive wall pressures (+0.2 to +0.6 mbar), consistent

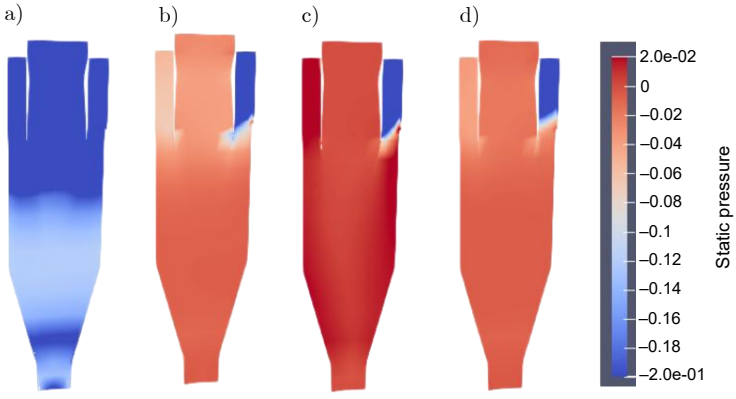

Fig. 7. Contours of static pressure [kPa] inside the cyclone obtained from CFD simulations for four different inlet velocity schemes: a) scheme 1, b) scheme 2, c) scheme 3, and d) scheme 4.

with incipient swirl development. Case 2 forms a more distinct Rankine-type vortex with wall pressures up to +1.2 mbar. Case 3 shows stronger wall pressure accumulation (up to +2.0 mbar) and a moderately negative core (−0.2 to −0.4 mbar), reflecting a mature, energetic swirl. In case 4, the maximum wall pressures exceed +2.5 mbar, while the core remains negative (−0.4 to −0.6 mbar), indicating vortex compression and substantial turbulence production.

Integrating these observations, the pressure drop along the helical pipe clearly increases with inlet velocity, ranging from 0.902 kPa at 7 m/s to 6.540 kPa at 20 m/s, while the internal cyclone velocity may paradoxically decrease at higher inlet momentum due to turbulence-dominated dissipation. The system transitions from weak to fully developed swirl as inlet velocity increases, evidenced by progressively stronger wall pressures and moderately negative core pressures. These findings confirm that the helical pipe is the dominant contributor to total pressure losses, particularly at high inlet velocities where curvature and turbulence interact synergistically. For pyrolysis heat-recovery applications, inlet velocities corresponding to case 3 or lower are recommended to maintain a stable swirl while avoiding excessive pressure penalties. These observed phenomena – including Dean vortex formation, curvature-induced secondary flows, and turbulence-dominated energy dissipation – are consistent with previous studies on swirling flows in curved pipes and confined cyclones.

3.2. CFD-ANN

In this study, the architecture and topology parameters of the CFD-ANN were determined using a hybrid method based on personal experience and a trial-and-error approach. Several different CFD-ANN models were tested to meet specific criteria, where all errors, measured as mean absolute errors (MAE) for the training and validation datasets, had to be below 5 %. This criterion emphasizes the importance of achieving high accuracy in the proposed model. Table 3 illustrates the results of the CFD-ANN model analysis employing various config-

Table 3. CFD-ANN topology.

No	Number of hidden layers	Number of neurons per layer	Activation function	Optimizer	Learning rate	Batch size	MSE-training	MSE-validation
1	1	128	ReLU	Adam	0.0001	16	0.3837	0.5313
2	1	64	ReLU	Adam	0.0001	16	0.4627	0.5319
3	2	128-64	ReLU	Adam	0.0001	16	0.1823	0.2391
4	2	64-32	ReLU	Adam	0.0001	16	0.2433	0.3213
5	3	128-64-64	ReLU	Adam	0.0001	16	0.0020	0.0019
6	3	128-64-32	ReLU	Adam	0.0001	16	0.0033	0.0040

urations of neural networks in an effort to optimize predictions. Each model was evaluated based on several parameters, including the number of hidden layers, the number of neurons per layer, activation function, optimization algorithm, learning rate, batch size, and MSE for both training and validation datasets. By assessing the resulting errors, the authors aimed to identify the most effective model configuration for capturing patterns in the data while maintaining the ability to generalize well to previously unseen data. Key parameters in this table include the number of hidden layers, which varied between one to three layers and the number of neurons per layer, which also varied (128, 64, and 32). All models utilized the ReLU activation function, known for its ability to accelerate convergence during training. Additionally, all models employed the Adam optimization algorithm with a learning rate of 0.0001 and a batch size of 16. The use of these parameters was expected to yield optimal results in both the training and validation processes.

The results of the analysis revealed that the model with a single hidden layer and 128 neurons yielded an MSE of 0.3837 for the training data and an MSE of 0.5313 for the validation data. This indicates that, although the model was able to learn the training data adequately, its capacity to generalize to new data was still limited. The second model, which used a single hidden layer with 64 neurons, exhibited worse results, with a training MSE of 0.4627 and a validation MSE of 0.5319, suggesting that reducing the number of neurons could potentially diminish the model's ability to capture the necessary information. In contrast, the model with two hidden layers (model 3) and a configuration of 128-64 neurons demonstrated a significant improvement, with a training MSE of 0.1823 and a validation MSE of 0.2391. This suggests that the addition of hidden layers can enhance the model's ability to capture the complexity of the data. The fourth model, which also employed two layers but with a configuration of 64-32 neurons, showed lower performance with a higher validation MSE of 0.3213, underscoring the importance of selecting an appropriate number of neurons to ensure that the model possesses sufficient capacity. Models 5 and 6, both utilizing three hidden layers, exhibited exceptional performance. Model 5, with a configuration of 128-64-64, achieved remarkably low MSEs for both training (0.0020) and validation (0.0019), indicating outstanding generalization capability. Model 6, with a configuration of 128-64-32, also demonstrated good performance, with a training MSE of 0.0033 and a validation MSE of 0.0040. These results signify that deeper models with an appropriate combination of neurons possess higher potential for learning and generalizing data, which is crucial in CFD-ANN applications.

Figure 8 illustrates the training and validation loss of an ANN over 100 epochs. Initially, both the training loss (blue line) and validation loss (orange line) are relatively high, but they rapidly decrease within the first 10 epochs, indicating

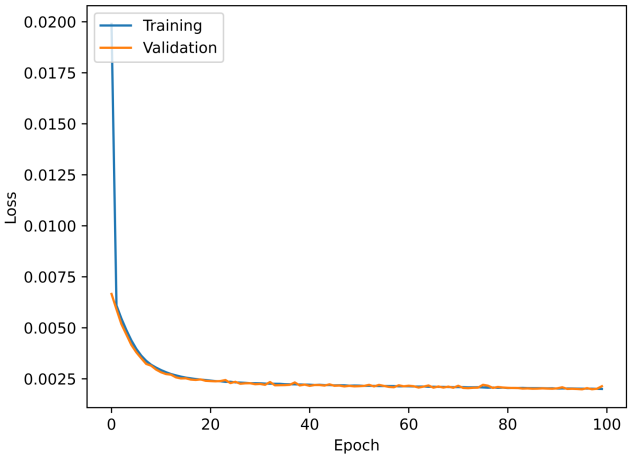

FIG. 8. Training and validation loss curves of the ANN.

that the model quickly learns to minimize error. After this steep decline, the loss values for both training and validation stabilize and remain nearly constant beyond 20 epochs. This suggests that the model has effectively converged and that additional training does not significantly improve performance. Importantly, the close alignment between the training and validation loss curves indicates that the model is not overfitting; it performs well on both the training data and unseen validation data. The final low-loss values reflect the model's strong ability to generalize to new data, demonstrating that it has learned the underlying patterns effectively.

Figure 9 provides a comparative assessment between CFD ground-truth data and ANN-predicted values for the velocity components U_x, U_y, U_z and the static pressure p along the helical pipe. The results show that the ANN exhibits excellent predictive performance for pressure, as indicated by the near-complete overlap between predicted and actual values. This close agreement suggests that the model effectively captures the dominant pressure gradient induced by axial flow, curvature effects, and the relatively smooth pressure field distribution, which tends to be easier for data-driven models to learn and generalize. In contrast, the ANN displays noticeably reduced accuracy for the velocity components. Although the predicted U_x, U_y, and U_z trends broadly follow the CFD data, the model fails to reproduce sharp spatial gradients and local fluctuations. Deviations become most evident in zones dominated by secondary flows, Dean vortices, and curvature-driven acceleration – regions where the velocity field exhibits strong nonlinearity and multiscale behavior typical of helical and rotating passages.

These limitations can be explained by several factors. First, velocity fields in helical geometries are highly sensitive to geometric curvature and centrifugal

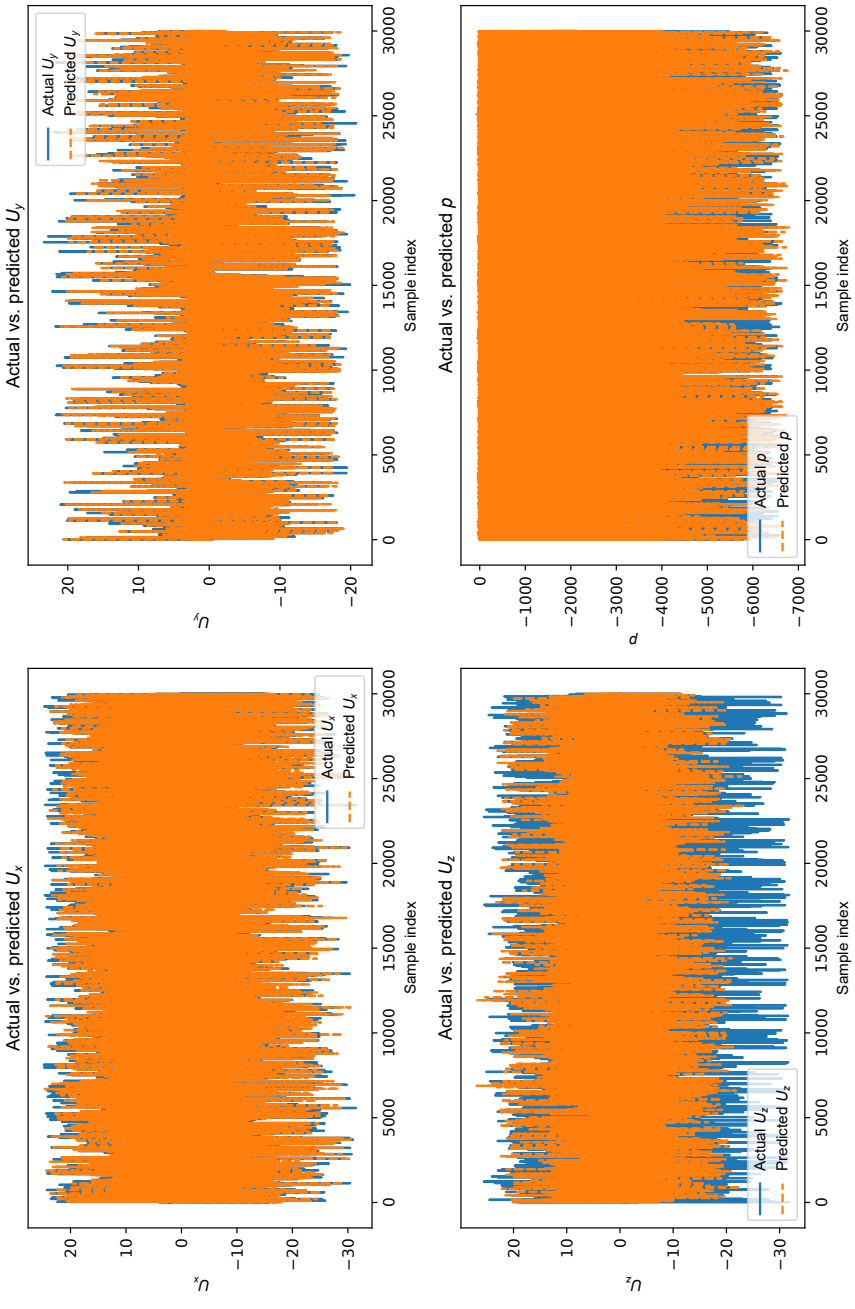

Fig. 9. Comparison of actual vs. predicted values for velocity and pressure field.

effects, making their distribution substantially more complex than the comparatively smoother pressure field. Second, the training dataset may insufficiently represent high-gradient regions (e.g., near walls or vortex cores), causing the ANN to underfit complex features while preferentially learning smoother regions. Third, the fully connected architecture employed in this study may lack the capacity to capture the multiscale nature of the fluctuating velocity field.

Such challenges are well documented in recent data-driven turbulence modeling studies. Beck *et al.* [27] reported that while DNNs can perform effectively as LES closure models, their ability to reconstruct fine-scale turbulence remains limited without additional constraints or specialized architectures. Similarly, PINNs, which integrate Navier–Stokes residuals into the learning process, have shown improved physical consistency for velocity predictions by enforcing mass and momentum conservation [28].

Several strategies may enhance the ANN's predictive capability for velocity components. Augmenting the training dataset with more samples from regions exhibiting high gradients would allow the model to better learn complex motion structures. Incorporating architectures that account for spatial correlations, such as convolutional neural networks (CNNs), could improve the capture of coherent flow patterns – an approach that has demonstrated success in data-driven urban wind-flow prediction [29]. Furthermore, embedding physical constraints through PINNs or energy-preserving neural frameworks may reduce non-physical artifacts and improve prediction robustness, as highlighted in recent developments in physics-constrained turbulence modeling [30].

4. Conclusions

This study presented a hybrid CFD-ANN framework for predicting the full three-dimensional velocity and static pressure fields in a cyclone separator with a helical inlet. CFD simulations revealed that pressure drop along the helical pipe increases nonlinearly with inlet velocity, ranging from 0.902 kPa at 7 m/s to 6.540 kPa at 20 m/s, primarily due to curvature-induced secondary flows, Dean vortex formation, and enhanced wall friction. Interestingly, the magnitude of velocity within the cyclone exhibited a counterintuitive trend: although the inlet momentum increased, turbulent dissipation and wall interactions reduced the effective core velocity, with peak velocities near the core decreasing to 1–2 m/s at the highest inlet speed. These findings illustrate the complex interplay between swirl development, turbulence, and pressure evolution within confined swirling flows. The ANN surrogate, trained on CFD-generated datasets, successfully reproduced the pressure field with high fidelity, achieving near-perfect agreement with CFD predictions and enabling rapid estimation of cyclone performance within milliseconds. The velocity components were predicted with reasonable

accuracy; however, high-gradient regions associated with secondary flows and vortex cores remained challenging, highlighting the need for enriched datasets or physics-informed enhancements for more precise flow reconstruction. Collectively, the integrated CFD-ANN approach provides a computationally efficient tool for rapid design iteration, performance optimization, and sensitivity analysis in cyclone systems. Practically, the results suggest that maintaining inlet velocities corresponding to moderate operating conditions (e.g., 7–13 m/s) can balance swirl development and pressure drop, ensuring effective particle separation while limiting energy consumption. Future work may focus on incorporating additional geometric variations, particle-laden flows, and physics-constrained machine-learning architectures to further enhance predictive capability and industrial applicability.

Acknowledgments

This research was supported by the Program Bantuan Operasional Perguruan Tinggi Negeri Fundamental Research Program for Fiscal Year 2024 under contract no. NKB-919/UN2.RST/HKP.05.00/2024.

References

1. Cooper C.D., Alley F.C., *Air Pollution Control: A Design Approach*, Waveland Press, Long Grove, IL, 2011.

2. Baburaj P.P., Abhilash S., Nirmal C.S.A., Sreenath A.V., Mohankumar K., Sahai A.K., Increasing incidence of Arabian Sea cyclones during the monsoon onset phase: Its impact on the robustness and advancement of Indian summer monsoon, *Atmospheric Research*, **267**: 105915, 2022, https://doi.org/10.1016/j.atmosres.2021.105915.

3. Akhbarifar S., Shirvani M., Improving cyclone efficiency for small particles, *Chemical Engineering Research & Design*, **147**: 483–492, 2019, https://doi.org/10.1016/j.cherd.2019.05.026.

4. Chen J., Shi M., A universal model to calculate cyclone pressure drop, *Powder Technology*, **171**(3): 184–191, 2007, https://doi.org/10.1016/j.powtec.2006.09.014.

5. Soliman M.M., El-shaer Y., Elsayed K., Ibrahim M.A., Performance enhancement of gas cyclone with streamlined ports using CFD simulations, *Journal of Engineering and Applied Science*, **72**: 4, 2025, https://doi.org/10.1186/s44147-024-00575-8.

6. Brar L.S., Rahmani F., The impact of operating temperatures on the fluctuating flow field and precessing vortex core in cyclone separator using large-eddy simulations, *Physics of Fluids*, **36**(3): 33335, 2024, https://doi.org/10.1063/5.0195382.

7. Wasilewski M., Singh Brar L., Ligus G., Effect of the central rod dimensions on the performance of cyclone separators – optimization study, *Separation and Purification Technology*, **274**: 119020, 2021, https://doi.org/10.1016/j.seppur.2021.119020.

8. Parvaz F. *et al.*, Influence of gas exhaust geometry on flow pattern, performance, and erosion rate of a gas cyclone, *Korean Journal of Chemical Engineering*, **40**(7): 1587–1597, 2023, https://doi.org/10.1007/s11814-023-1430-2.

9. de Oliveira J.P.S., Alves J.V.B., Carneiro J.N.E., de Andrade Medronho R., Silva L.F.L.R., Coupling a neural network technique with CFD simulations for predicting 2-D atmospheric dispersion analyzing wind and composition effects, *Journal of Loss Prevention in the Process Industries*, **80**: 104930, 2022, https://doi.org/10.1016/j.jlp.2022.104930.

10. Le D.K., Yoon J.Y., A hybrid CFD – Deep learning methodology for improving the accuracy of pressure drop prediction in cyclone separators, *Chemical Engineering Research & Design*, **190**: 296–311, 2023, https://doi.org/10.1016/j.cherd.2022.12.035.

11. Pandey S. *et al.*, CFD investigations of cyclone separators with different cone heights and shapes, *Applied Sciences*, **12**(10): 4904, 2022, https://doi.org/10.3390/app12104904.

12. Pechmanee P., Namkanisorn A., Wattananusorn S., Bumrungthaichaichan E., CFD simulations of high efficiency gas cyclones: An influence of dustbin geometry, *Computer Aided Chemical Engineering*, **50**: 529–534, 2021.

13. Cai S., Mao Z., Wang Z., Yin M., Karniadakis G.E., Physics-informed neural networks (PINNs) for fluid mechanics: A review, *Acta Mechanica Sinica*, **37**(12): 1727–1738, 2021, https://doi.org/10.1007/s10409-021-01148-1.

14. Gronald G., Derksen J.J., Simulating turbulent swirling flow in a gas cyclone: A comparison of various modeling approaches, *Powder Technology*, **205**(1–3): 160–171, 2011, https://doi.org/10.1016/j.powtec.2010.09.007.

15. Meza H.Z., Margarita L., Application of computational fluid dynamics to study the influence of turbulence models in the behavior of the cyclonic separators, *International Journal of Petrochemical Science & Engineering*, **2**(2): 66–72, 2017, https://doi.org/10.15406/ipcse.2017.02.00033.

16. Nakhaei M., Lu B., Tian Y., Wang W., Dam-Johansen K., Wu H., CFD modeling of gas–solid cyclone separators at ambient and elevated temperatures, *Processes*, **8**(2): 228, 2020, https://doi.org/10.3390/pr8020228.

17. Tankari S., Halder P., Franklin E., Aravalli K., CFD analysis of a cyclone seperator, **2**(09): 322–327, 2014, https://api.semanticscholar.org/CorpusID:110099480.

18. De Santis G., De Beule M., Van Canneyt K., Segers P., Verdonck P., Verhegghe B., Full-hexahedral structured meshing for image-based computational vascular modeling, *Medical Engineering and Physics*, **33**(10): 1318–1325, 2011, https://doi.org/10.1016/j.medengphy.2011.06.007.

19. Xu K., Gao X., Chen G., Hexahedral mesh quality improvement via edge-angle optimization, *Computers & Graphics*, **70**: 17–27, 2018, https://doi.org/10.1016/j.cag.2017.07.002.

20. Gharbi R., Estimating the isothermal compressibility coefficient of undersaturated Middle East crudes using neural networks, *Energy & Fuels*, **11**(2): 372–378, 1997, https://doi.org/10.1021/ef960123y.

21. Dhakane V., Mishra P., Yadav A., Computational fluid dynamics (CFD) – deep neural network (DNN) model to predict hydrodynamic parameters in rectangular and cylindrical bubble columns, *Digital Chemical Engineering*, **13**: 100185, 2024, https://doi.org/10.1016/j.dche.2024.100185.

22. Kaak A.R.S., Çelebioğlu K., Bozkuş Z., Ulucak O., Ayli E., A novel CFD-ANN approach for plunger valve optimization: Cost-effective performance enhancement, *Flow Measurement and Instrumentation*, **97**: 102589, 2024, https://doi.org/10.1016/j.flowmeasinst.2024.102589.

23. Diop M., Dubois P., Toubin H., Planckaert L., Le Roy J.-F., Garnier E., Reconstruction of flow around a high-rise building from wake measurements using Machine Learning techniques, *Journal of Wind Engineering and Industrial Aerodynamics*, **230**: 105149, 2022, https://doi.org/10.1016/j.jweia.2022.105149.

24. Tian J., Gurley K.R., Diaz M.T., Fernández-Cabán P.L., Masters F.J., Fang R., Low-rise gable roof buildings pressure prediction using deep neural networks, *Journal of Wind Engineering and Industrial Aerodynamics*, **196**: 104026, 2020, https://doi.org/10.1016/j.jweia.2019.104026.

25. Gupta A., Roy S., Euler–Euler simulation of bubbly flow in a rectangular bubble column: Experimental validation with radioactive particle tracking, *Chemical Engineering Journal*, **225**: 818–836, 2013, https://doi.org/10.1016/j.cej.2012.11.012.

26. Das L., Sivaram A., Venkatasubramanian V., Hidden representations in deep neural networks: Part 2. Regression problems, *Computers & Chemical Engineering*, **139**: 106895, 2020, https://doi.org/10.1016/j.compchemeng.2020.106895.

27. Beck A., Flad D., Munz C.-D., Deep neural networks for data-driven LES closure models, *Journal of Computational Physics*, **398**: 108910, 2019, https://doi.org/10.1016/j.jcp.2019.108910.

28. Eivazi H., Tahani M., Schlatter P., Vinuesa R., Physics-informed neural networks for solving Reynolds-averaged Navier–Stokes equations, *Physics of Fluids*, **34**(7): 075117 2022, https://doi.org/10.1063/5.0095270.

29. Zhao R., Zhong S., You R., Application of convolutional neural network for efficient turbulence modeling in urban wind field simulation, *Physics of Fluids*, **36**(10): 105169, 2024, https://doi.org/10.1063/5.0233053.

30. van Gastelen T., Edeling W., Sanderse B., Energy-conserving neural network for turbulence closure modeling, *Journal of Computational Physics*, **508**: 113003, 2024, https://doi.org/10.1016/j.jcp.2024.113003.

Received April 22, 2025; revised November 24, 2025; accepted May 14, 2026; version of record June 25, 2026.